Study of the citral/acetone reaction on Mg$_y$AlO$_x$ oxides: Effect of the chemical composition on catalyst activity, selectivity and stability

V.K. Díez, J.I. Di Cosimo, C.R. Apesteguía *

Catalysis Science and Engineering Research Group (GICIC), Instituto de Investigaciones en Catálisis y Petroquímica - INCAPE-(UNL-CONICET), Santiago del Estero 2654, (3000) Santa Fe, Argentina

A R T I C L E   I N F O

A B S T R A C T

The liquid-phase citral/acetone reaction was studied on MgO, Al$_2$O$_3$ and Mg$_y$AlO$_x$ mixed oxides with Mg/Al molar ratios of 0.11–3. The density, strength and nature of surface acid sites were determined by NH$_3$ thermodesorption and FTIR of pyridine. The surface basic properties were probed by temperature-programmed desorption of CO$_2$. The rate of the citral/acetone cross-aldolization to pseudoionones increased linearly with the density of strong O^{2-} base sites. Thus, the pseudoionone synthesis was efficiently promoted on MgO and Mg-rich Mg$_y$AlO$_x$ samples. In contrast, the initial rate of the parallel acetone self-condensation reaction increased with the density of Lewis acid sites, and diacetone alcohol was more rapidly formed on Al$_2$O$_3$ and Al-rich Mg$_y$AlO$_x$ samples. Differences in the reactant adsorption strength on surface Al^{3+} sites may explain the observed differences between the acid-catalyzed mechanisms of cross- and self-aldolization reactions. In situ catalyst deactivation was determined by performing two consecutive catalytic runs. The activity decay of Mg$_y$AlO$_x$ samples during the citral/acetone reaction was between 15 and 20%, irrespective of the catalyst composition.

© 2008 Elsevier B.V. All rights reserved.

1. Introduction

Pseudoionones (6,10-dimethyl-3,5,9-undeca-trien-2-one) are valuable acyclic intermediates for the synthesis of α-, β- and γ-ionones which are extensively used as pharmaceuticals and fragrances. Specifically, β-ionone is an important precursor in the synthesis of vitamin A whereas α- and γ-ionones are in high demand in the fragrance industry because of their violet and woody-fruity scent, respectively [1,2]. Ionones are commercially produced from acetone and citral (3,7-dimethyl-2,6-octadienal), using homogeneous catalysis via a two-step process, as depicted in Scheme 1. Initially, the liquid-phase aldol condensation of citral with acetone is catalyzed by diluted bases, such as NaOH, Ba(OH)$_2$ or LiOH, and forms selectively pseudoionones [3,4]. The consecutive cyclization of pseudoionones to yield ionone isomers is catalyzed by strong liquid acids [5]. Because of the use of harmful liquid catalysts, the global process entails concerns related to high toxicity, corrosion, and disposal of spent acid and base materials.

New industrial strategies for ionone synthesis demand then the replacement of liquid acids or bases by solid catalysts.

In particular, considerable effort has been devoted to the development of recyclable solid catalysts for efficiently promoting the liquid-phase aldol condensation of citral with acetone to produce pseudoionones. Aldol condensation of aldehydes and ketones are important reactions in organic synthesis because they form C–C bonds. Although aldolizations are promoted by a large variety of solid acids and bases, the desired selectivity is not frequently obtained because of the simultaneous formation of secondary unwanted products. The reaction of citral with acetone is a cross-aldolization reaction but the self-aldolization of acetone to yield diacetone alcohol may simultaneously occur. Liquid-phase conversion of acetone to diacetone alcohol is limited by thermodynamics [6], but diacetone alcohol is easily dehydrated to mesityl oxide in presence of acid catalysts. Previous work [7], showed that the citral/acetone reaction is poorly catalyzed by acid zeolites or bifunctional acid–base aluminophosphates (ALPO). In contrast, rehydrated Mg–Al hydrotalcites with Mg/Al ratio between 2 and 3 may selectively produce pseudoionones [8–11]; however, the industrial use of these catalytic materials is seriously hindered because they are unstable in air. Alkaline-doped MgO also promotes efficiently the selective formation of pseudoionones [12,13]. We have recently shown, in fact, that MgO doped with

* Corresponding author. Tel.: +54 342 4555279; fax: +54 342 4531068.
E-mail address: capesteg@fiqus.unl.edu.ar (C.R. Apesteguía).
URL: http://www.ceride.gov.ar/gicic
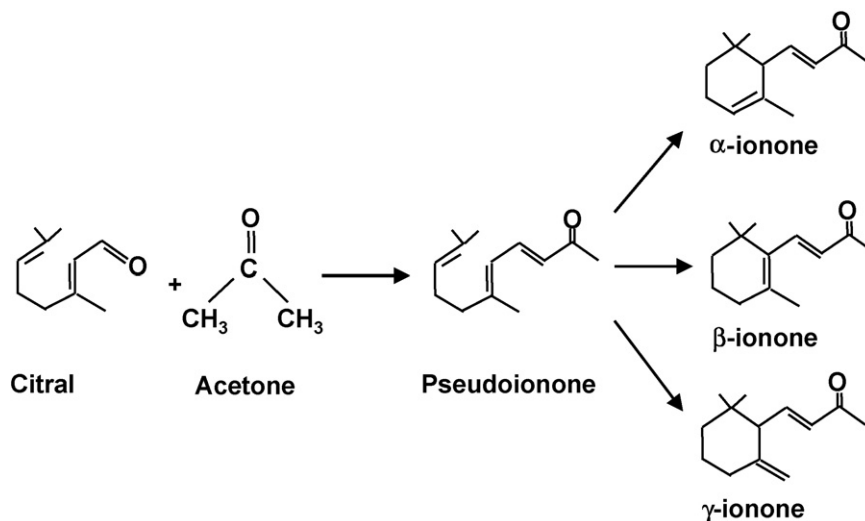
Scheme 1. Reaction sequence for ionone synthesis from citral/acetone reaction.

0.5 wt.% Li yields 93% of pseudoionones at 353 K using a catalyst/citral weight ratio of 0.2 [13].

Other authors have studied the citral/acetone reaction on Mg–Al mixed oxides (Mg_yAlO_x) [7,14–16]. These materials catalyze a variety of reactions requiring anionic intermediates, such as the self-condensation of acetone [17], alkylations [18], Knoevenagel condensations [19], Michael additions [20], cyanoethylation of alcohols [21], and double-bond isomerization of alkenes [22]. We have also investigated the use of Mg_yAlO_x catalysts to promote several reactions involving primary and secondary alcohols, such as the self-condensation of ethanol [23], the cross-coupling of methanol and 1-propanol [24], and the one-step synthesis of methyl isobutyl ketone from 2-propanol [25]. The density and strength of surface acid/base sites on Mg_yAlO_x mixed oxides may be easily tuned by changing the chemical composition, i.e., the Mg/Al atomic ratio, and this explains the ability of these materials for catalyzing a variety of chemical reactions. Intermediate Mg/Al ratios lead to optimum catalytic properties for several reactions [17,26,27], but the optimum Mg/Al ratio depends on the specific requirements of base/acid site density and strength to enhance the rate and selectivity for each reaction. The catalytic properties of Mg_yAlO_x oxides for the citral/acetone reaction have been investigated [7,14–16] only on a restricted Mg/Al ratio range, between 2 and 4, probably because for this concentration range the parent Mg_yAlO_x precursors appear in a single crystalline hydrotalcite structure [27]. Thus, knowledge regarding the role played by the chemical composition of Mg_yAlO_x mixed oxides to fulfill the requirements of acid/base site density and strength for promoting the selective formation of pseudoionones at high rates is lacking. The optimum Mg_yAlO_x composition should improve the citral/acetone cross-aldol condensation rate at the expense of the acetone self-condensation reaction. Moreover, no studies have been performed on the deactivation of Mg_yAlO_x samples during the citral/acetone reaction, in spite that the catalyst stability is a key factor for evaluating the commercial development of catalytic materials.

Here, we have carried out a detailed study of the citral/acetone reaction on MgO, Al_2O_3 and Mg_yAlO_x mixed oxides with Mg/Al molar ratios of 0.11–3. The goals were: (i) to ascertain the effect of chemical composition on the generation of surface acid/base sites, (ii) to establish the effect of chemical composition on the complete reaction mechanism, i.e., the parallel pathways required for self- and cross-aldol condensations of the reactants, (iii) to study the catalyst deactivation by performing consecutive catalytic tests.

2. Experimental

2.1. Catalyst preparation

Mg–Al hydroxycarbonate precursors with Mg/Al atomic ratios (y) between 0.11 and 3 were prepared by co-precipitation. An acidic solution of the metal nitrates with a total [Al + Mg] cation concentration of 1.5 M was contacted with an aqueous solution of KOH and K_2CO_3 at a constant pH of 10. The two solutions were simultaneously added dropwise to 300 ml of distilled water that was maintained at a temperature of 333 K in a stirred batch reactor. The resulting precipitates were aged for 2 h at 333 K in their mother liquor and then filtered, washed thoroughly with 1000 ml of deionized water at 373 K, and dried at 353 K overnight. The residual potassium content in the mixed oxides samples was below 0.1 wt.%. Precursors were then decomposed in N_2 at 673 K overnight in order to obtain the corresponding Mg–Al mixed oxides (Mg_yAlO_x samples). Pure alumina and MgO were prepared following the same procedure.

2.2. Catalyst characterization

The crystalline structure of the Mg–Al hydroxycarbonate precursors and of the Mg–Al mixed oxides were determined via X-ray diffraction (XRD) using a Shimadzu XD-D1 diffractometer and Ni-filtered Cu Kα radiation. BET surface areas (S_g) were measured by N_2 physisorption at its boiling point using a Quantachrome Nova-1000 sorptometer. Elemental compositions were measured by atomic absorption spectroscopy (AAS).

CO_2 adsorption site densities and binding energies were obtained from temperature-programmed desorption (TPD) of CO_2 preadsorbed at room temperature. Samples (50–150 mg) were treated in N_2 at 673 K for 1 h and then exposed to a 3.09% CO_2/N_2 stream until saturation coverages were reached. Weakly adsorbed CO_2 was removed by flushing with N_2 at room temperature for about 1 h. The temperature was then increased at a rate of 10 K/min from 298 to 673 K. The desorbed CO_2 was converted to methane by means of a methanation catalyst (Ni/Kieselghur) operating at 673 K and monitored using a flame ionization detector.

Acid site densities were determined using TPD of NH_3 preadsorbed at room temperature. Samples (150 mg) were treated

in He ($\sim$100 cm^3/min) at 673 K for 0.5 h and then exposed to a 1.01% NH$_3$/He stream at 298 K until surface saturation. Weakly adsorbed NH$_3$ was removed by flushing He at 60 cm^3/min for 0.5 h. Afterward, the temperature was increased from 298 to 673 K at 10 K/min, and the NH$_3$ concentration in the effluent was measured by mass spectrometry using a Baltzers Omnistar unit.

The nature of surface acid sites was determined by infrared spectroscopy (IR) using pyridine as a probe molecule and a Shimadzu FTIR-8101M spectrophotometer. The spectral resolution was 4 cm^{-1} and 50 scans were added. Sample wafers were formed by pressing 20–40 mg of the catalyst at 5 ton/cm^2 and transferred to a sample holder made of quartz. An inverted T-shaped Pyrex cell containing the sample wafer was used. The two ends of the short arm of the T were fitted with CaF$_2$ windows. All the samples were initially outgassed in vacuum at 673 K for 4 h and then a background spectrum was recorded after cooling the sample at room temperature. Spectra were recorded at room temperature, after admission of pyridine, adsorption at room temperature and sequential evacuation at 298 and 423 K.

2.3. Catalytic testing

The cross-aldol condensation of citral (Millennium Chemicals, 95% geranial + neral) with acetone, DMK (Merck, PA) was carried out at 353 K under autogenous pressure ($\approx$250 kPa) in a batch Parr reactor, using a DMK/citral = 49 molar ratio and a catalyst/(citral + DMK) = 1 wt.% ratio. The liquid reactants were introduced first and then the reactor was flushed with nitrogen. Catalysts were pre-treated ex situ in flowing N$_2$ at 673 K for 2 h to remove adsorbed water and carbon dioxide and then quickly transferred to the reactor without exposing them to air. The batch reactor was assumed to be perfectly mixed. Inter- and intra-particle diffusional limitations were verified to be negligible. Reaction products were analyzed by gas chromatography in a Varian Star 3400 CX chromatograph equipped with an FID detector and a Carbowax Amine 30 M capillary column. Thirteen samples of the reaction mixture were extracted and analyzed during the 6-h reaction. The main reaction product of citral conversion was pseudoionone, PS (*cis*- and *trans*-isomers). Trace amounts of unidentified heavy compounds probably coming from self-condensation of citral were also obtained. Diacetone alcohol (DAA) and mesityl oxide (MO) formed from self-condensation of acetone were also detected in the reaction mixture. Selectivities of citral-derived products (S_i, mol of product i/mol of citral reacted) were calculated as $S_i = C_i/\sum C_i$ where C_i is the concentration of product i. Yields (η_i, mol of product i/mol of citral fed) were calculated as $\eta_i = S_i X_{\text{Cit}}$, where X_{Cit} is the citral conversion. Similar calculations apply for DMK-derived products.

3. Results and discussion

3.1. Structural and surface properties of Mg$_y$AlO$_x$ catalysts

The chemical composition, BET surface area and crystalline phases of the samples are shown in Table 1. The precipitated hydroxycarbonate precursors with r = Al/(Al + Mg) atomic ratios of 0.24 and 0.47 showed diffraction patterns consistent with the presence of a single crystalline hydrotalcite structure of Mg$_{1-r}$Al$_r$(OH)$_2$]$^{r+}$(CO$_3$)$_{r/2}^{2-}$·mH$_2$O composition. The stoichiometric hydrotalcite structure, Mg$_6$Al$_2$(OH)$_{16}$CO$_3$·4H$_2$O (ASTM 14-191) is reached when r is 0.25. For r ratios higher than 0.47, additional crystalline hydroxide phases of Mg [Mg(OH)$_2$, brucite, ASTM 7-239] or Al [Al(OH)$_3$, gibbsite, ASTM 7-324] were observed. No hydrotalcite phase was detected in precursors with $r \geq 0.83$.

Thermal decomposition of hydroxycarbonate precursors evolve CO$_2$ and H$_2$O that leads to the formation of high surface area Mg$_y$AlO$_x$ mixed oxides (130–300 m^2/g). The Al/(Al + Mg) atomic ratios of Mg$_y$AlO$_x$ samples were very similar to those present in the precursor solution, suggesting that Mg and Al salts precipitated completely during synthesis. The diffraction patterns of Mg-rich mixed oxides ($r \leq 0.5$) showed the presence of a single crystalline MgO periclase phase (ASTM 4-0829) with no residual traces of hydrotalcite or hydroxide phases, thereby indicating that heating at 673 K completely decomposes the precursor samples. The crystallinity of the MgO phase decreased with increasing r from 0 to 0.5. No crystalline AlO$_x$ phases were observed on Mg-rich mixed oxides ($r \leq 0.5$), which suggests that the Al^{3+} cations remained closely associated within the MgO structure after thermal decomposition of precipitated precursors. In Mg$_y$AlO$_x$ samples of high Al content ($r > 0.5$), a quasi-amorphous Al$_2$O$_3$ phase (ASTM 10-425) was detected, suggesting that Al^{3+} cations lost the intimate contact with the MgO matrix. In sample Mg$_{0.5}$AlO$_x$ (r = 0.67), an additional MgAl$_2$O$_4$ spinel phase (ASTM 21-1152) was also found showing the transition between Mg-rich and Al-rich catalysts. These results are consistent with our previous studies [27] that relate the homogeneity of Mg$_y$AlO$_x$ mixed oxides with the phase composition of parent co-precipitated precursors. In fact, we observed [27] that the decomposition of Mg-rich hydrotalcite-like precursors leads to homogeneous Mg$_y$AlO$_x$ mixed oxides containing the Al^{3+} cations totally incorporated into the MgO framework. In contrast, Al-rich co-precipitated precursors contain the Mg^{2+} and Al^{3+} cations in separate brucite and gibbsite hydroxide phases, and generate heterogeneous Mg$_y$AlO$_x$ mixed oxides, all of them containing separate low-crystallinity magnesia and alumina phases.

The base site density of the samples was obtained by TPD of CO$_2$ preadsorbed at room temperature. The CO$_2$ desorption rate as a function of sample temperature is presented in Fig. 1 for MgO,

Table 1
Chemical composition, BET surface areas and XRD characterization of MgO, Al$_2$O$_3$ and Mg$_y$AlO$_x$ mixed oxides

| Catalyst	r = Al/(Al + Mg) (nominal)	Chemical analysis[a]			S_g (m^2/g)	Phases detected by XRD	
		r	Mg (wt.%)	Al (wt.%)		Coprecipitated precursors	Mixed oxides
MgO	0.00	0.00	–	–	127	Brucite	MgO
Mg$_3$AlO$_x$	0.25	0.24	34.4	12.1	202	Hydrotalcite	MgO
Mg$_1$AlO$_x$	0.50	0.47	24.3	23.6	202	Hydrotalcite	MgO
Mg$_{0.5}$AlO$_x$	0.67	0.66	13.0	27.6	296	Hydrotalcite + brucite + gibbsite	MgO + MgAl$_2$O$_4$ + γ-Al$_2$O$_3$
Mg$_{0.33}$AlO$_x$	0.75	0.76	8.7	30.0	301	Brucite + gibbsite + hydrotalcite (t)	γ-Al$_2$O$_3$
Mg$_{0.2}$AlO$_x$	0.83	0.86	5.2	35.0	243	Brucite + gibbsite	γ-Al$_2$O$_3$
Mg$_{0.11}$AlO$_x$	0.90	0.91	3.4	37.4	240	Brucite (t) + gibbsite	γ-Al$_2$O$_3$
Al$_2$O$_3$	1.00	1.00	–	–	303	Gibbsite	γ-Al$_2$O$_3$

[a] By AAS; (t), traces.
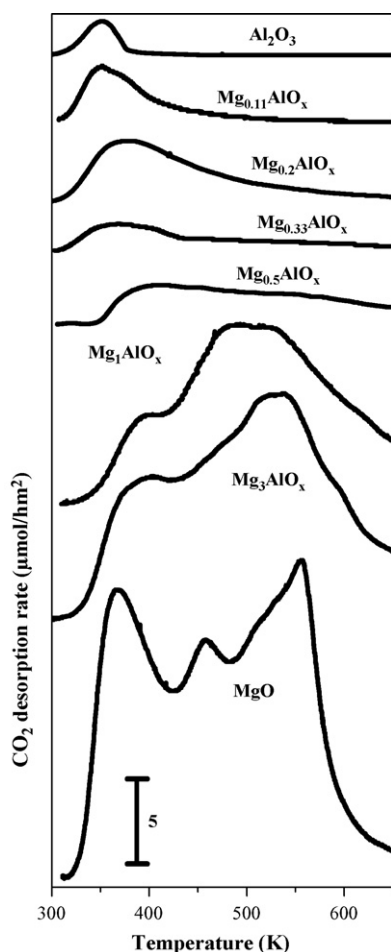
Fig. 1. TPD of CO_2 on Al_2O_3, Mg_yAlO_x and MgO samples. CO_2 adsorption at 298 K, heating rate: 10 K/min.

Al_2O_3 and Mg_yAlO_x samples. The complex TPD profiles of Fig. 1 suggest that the surface of the Mg_yAlO_x oxides are nonuniform and contain several species formed by CO_2 adsorption; in other words, the sample surfaces contain oxygen atoms of different chemical nature that bind CO_2 with different coordination and binding energy. In previous work [23], we investigated the chemical nature of the adsorbed species on similar alkaline-promoted MgO catalysts by using FTIR and identified at least three different CO_2 adsorption species: unidentate carbonate, bidentate carbonate and bicarbonate. Unidentate carbonate formation requires isolated surface O^{2-} ions, i.e., low-coordination anions, such as those present in corners or edges and exhibits a symmetric O–C–O

stretching at 1360–1400 cm^{-1} and an asymmetric O–C–O stretching at 1510–1560 cm^{-1}. Bidentate carbonate forms on Lewis acid–Brönsted base pairs (M^{n+}–O^{2-} pair site, where M^{n+} is the metal cation Mg^{2+} or Al^{3+}), and shows a symmetric O–C–O stretching at 1320–1340 cm^{-1} and an asymmetric O–C–O stretching at 1610–1630 cm^{-1}. Bicarbonate species formation involves surface hydroxyl groups and shows a C–OH bending mode at 1220 cm^{-1} as well as symmetric and asymmetric O–C–O stretching bands at 1480 cm^{-1} and 1650 cm^{-1}, respectively [28–30]. We also determined the following base strength order for these surface oxygen species: low coordination O^{2-} anions > oxygen in M^{n+}–O^{2-} pairs > OH groups [23].

Based on this previous IR characterization, the TPD profiles of Fig. 1 were deconvoluted in three desorption peaks: a low-temperature peak at 370–400 K, assigned to bicarbonates formed on Brönsted OH groups; a middle-temperature peak at 460 K attributed to bidentate carbonates desorbed from metal–oxygen pairs; and a high-temperature peak at 550 K resulting from unidentate carbonates released from low coordination oxygen anions. By integrating these three CO_2 TPD peaks we determined the density of weak (n_{OH}), middle (n_{MO}), and strong (n_O) base sites, respectively. Results are shown in Table 2. The highest total surface density of adsorbed CO_2 (n_b) was determined on MgO (5.89 μmol/m^2). The n_b value decreased with the addition of Al reaching a minimum on pure Al_2O_3 (0.11 μmol/m^2). Alumina is an amphoteric oxide and lacks strong base sites, but it contains surface sites capable of binding CO_2 with weak and intermediate strength, corresponding to surface OH groups and Al–O site pairs. Strongly basic O^{2-} sites and surface Mg–O pairs are dominant on MgO and Mg_yAlO_x samples with $r \leq 0.5$. In Al-rich samples ($r > 0.5$), the relative contribution of the high- and middle-temperature peaks decrease with increasing the Al content at the expense of the low-temperature peak. Pure Al_2O_3 and $Mg_{0.11}AlO_x$ samples showed no contribution of the high-temperature peak in their TPD profiles.

Sample acid properties were probed by TPD of NH_3 preadsorbed at 298 K. The obtained TPD curves are shown in Fig. 2. The NH_3 TPD profile on Al_2O_3 shows that NH_3 desorbed in two overlapping signals, a low-temperature peak at about 400 K and a high-temperature peak at 575 K. In Mg_yAlO_x oxides, the high-temperature peak drastically decreased with the diminution of the Al content in the sample. The surface densities of acid sites (n_a, μmol/m^2) were obtained by deconvolution and integration of NH_3 TPD profiles and are presented in Table 2. The total NH_3 desorbed from Mg_yAlO_x samples was similarly low on Mg-rich samples ($r \leq 0.5$), but increases almost linearly with increasing Al content on samples with $r > 0.5$.

The nature of surface acid sites on MgO, $Mg_{0.2}AlO_x$ and Al_2O_3 was determined from the FTIR spectra of adsorbed pyridine. Fig. 3 shows the spectra recorded after pyridine adsorption at 298 K

Table 2
Catalyst characterization: acid–base properties

Catalyst	Density of base sites [a] (μmol/m^2)				Density of acid sites[b] (μmol/m^2)
	Total n_b	Weak n_{OH}	Middle n_{MO}	Strong n_O	Total n_a
MgO	5.89	0.81	2.24	2.84	0.14
Mg_3AlO_x	4.70	0.60	0.90	3.30	0.19
Mg_1AlO_x	3.90	0.20	1.70	2.00	0.19
$Mg_{0.5}AlO_x$	1.00	0.30	0.40	0.30	0.28
$Mg_{0.33}AlO_x$	0.40	0.20	0.15	0.05	0.37
$Mg_{0.2}AlO_x$	0.70	0.30	0.20	0.20	0.43
$Mg_{0.11}AlO_x$	0.30	0.20	0.10	0.00	0.57
Al_2O_3	0.11	0.09	0.02	0.00	0.62

[a] TPD of adsorbed CO_2.
[b] TPD of adsorbed NH_3.
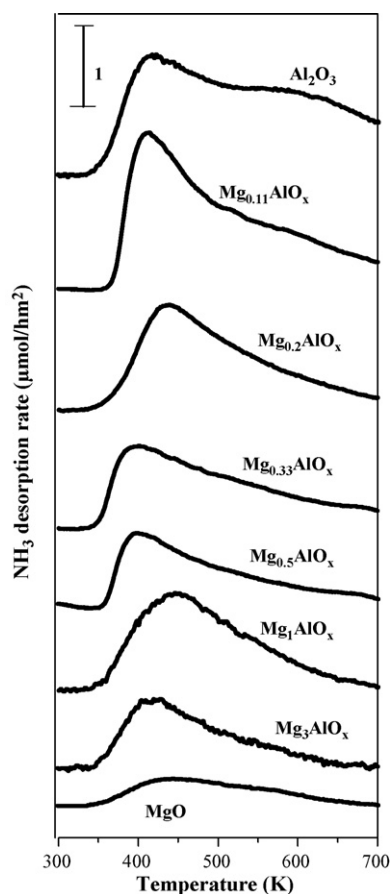
Fig. 2. TPD profiles of NH_3 on Al_2O_3, Mg_yAlO_x and MgO samples. NH_3 adsorption at 298 K, heating rate: 10 K/min.

and sequential evacuation at 298 and 423 K. The IR band assignment of the surface species arising from the adsorption of pyridine on alumina has been reported by several authors [31–34]. In agreement with these studies, the IR spectrum of adsorbed pyridine on Al_2O_3 in Fig. 3 does not exhibit the band at 1540 cm^{-1} characteristic of the formation of surface pyridinium ions. This result shows that alumina does not contain Brönsted acid sites strong enough to react with pyridine. The band at 1450 cm^{-1} corresponds to coordinatively bonded pyridine and typically reveals the presence of surface Lewis acid sites on alumina. Finally, the interaction of pyridine molecules via H-bonding with weakly acidic surface OH species (i.e., with weak Brönsted acid sites) gives rise to a band at about 1595 cm^{-1} [32,33]. IR spectra of Fig. 3 show that the most intense absorption band on pure alumina appears at 1450 cm^{-1} revealing that Al_2O_3 exhibits essentially Lewis acidity. Moreover, the band at 1450 cm^{-1} was still present after evacuation at 423 K thereby indicating that a significant amount of pyridine remained adsorbed on stronger Lewis acid sites. In contrast, the small band at 1595 cm^{-1} corresponding to pyridine H-bonded to surface OH species is completely eliminated by evacuation at 423 K confirming the weak acidity of the Brönsted sites on alumina. By comparison of pyridine spectra on Al_2O_3 and $Mg_{0.2}AlO_x$ samples in Fig. 3, it is inferred that the density of Lewis acid sites on $Mg_{0.2}AlO_x$ as measured by the band at 1450 cm^{-1} after evacuation at 423 K is lower than on alumina. This result reflects the diminution of the Lewis acid site strength caused by the replacement of Al^{3+} species by less electronegative Mg^{2+} ions. The concentration of strong Lewis acid sites is negligible on MgO.
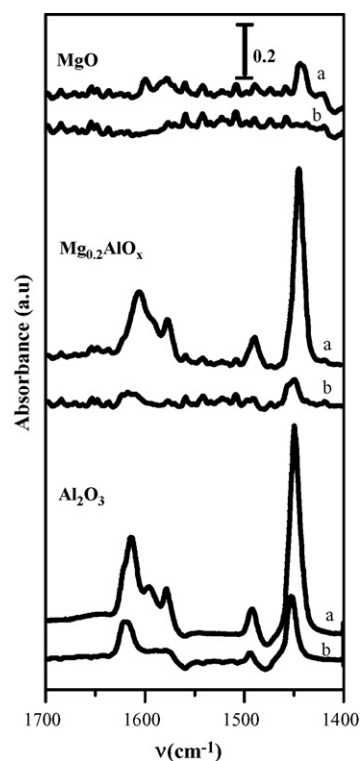

Fig. 3. FTIR spectra of pyridine adsorbed on Al_2O_3, $Mg_{0.2}AlO_x$ and MgO at 298 K and evacuated at 298 K (a) and 423 K (b) for 0.5 h.

3.2. Catalytic results on Mg_yAlO_x catalysts

Catalysts of Table 1 were tested for the citral/DMK reaction. Fig. 4 shows the citral conversion (X_{Cit}) and yields (η_i) as a function of time obtained at 353 K on Mg_3AlO_x and typically illustrates the catalyst behavior during the reaction. cis-PS and trans-PS isomers were the main products reaching together a yield of about 84% at 87% citral conversion after 6 h of reaction. The cis-PS/trans-PS ratio was about 1.3 during the entire catalytic test.

In Fig. 5 we have represented X_{Cit} as a function of parameter tW/n_{Cit}^0, where t is the reaction time, W is the catalyst weight, and n_{Cit}^0 are the initial moles of citral. The local slope of each curve in Fig. 5 gives the citral conversion rate at a specific value of citral conversion and reaction time. Thus, we determined the initial citral
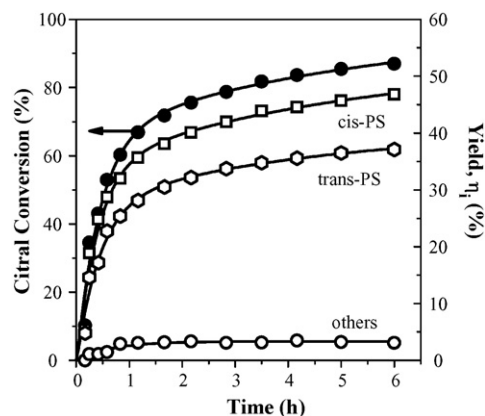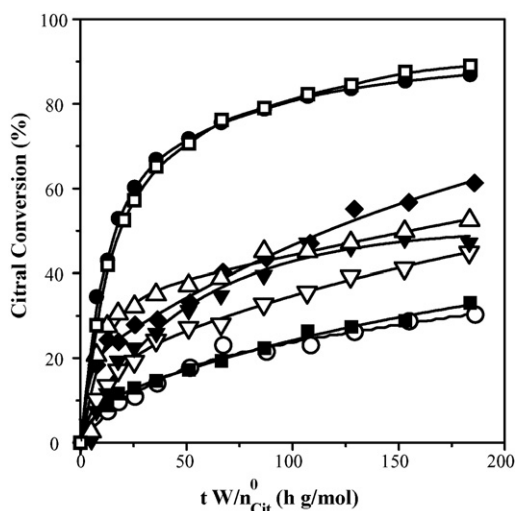

Fig. 4. Citral conversion and product yields as a function of time on Mg_3AlO_x sample (T = 353 K, n_{DMK}^0 = 0.8 mol, n_{Cit}^0 = 0.016 mol, $W_{Cat.}$ = 0.5 g).

Fig. 5. Citral conversion as a function of parameter tW/n_{Cit}^0 for MgO ($\square$), Mg_3AlO_x ($\bullet$), Mg_1AlO_x ($\triangle$), $Mg_{0.5}AlO_x$ ($\blacklozenge$), $Mg_{0.33}AlO_x$ ($\blacktriangledown$), $Mg_{0.2}AlO_x$ ($\triangledown$), $Mg_{0.11}AlO_x$, ($\blacksquare$) and Al_2O_3 ($\circ$) ($T = 353$ K, $n_{DMK}^0 = 0.8$ mol, $n_{Cit}^0 = 0.016$ mol, $W_{Cat.} = 0.5$ g).

conversion rate on an area basis (r_{Cit}^0, μmol/min m^2) by calculating the initial slopes in Fig. 5 according to

$$r_{Cit}^0 = \frac{1}{S_g}\left[\frac{dX_{Cit}}{d(tW/n_{Cit}^0)}\right]_{tW/n_{Cit}^0 = 0}$$

Results are given in Table 3 and show that MgO and Mg_3AlO_x were the most active catalysts at initial conditions. The r_{Cit}^0 values corresponding to Mg_yAlO_x samples diminished with the Al content. Similarly, the citral conversion after the 6 h catalytic tests decreased from near 90% on MgO and Mg_3AlO_x to 30.3% on pure alumina. In contrast, the selectivity to PS did not change with the Al loading reaching between 90 and 100% on all the samples (Table 3). The PS yield followed therefore the same trend that the citral conversion decreasing from about 85% on MgO and Mg_3AlO_x to 29.7% on alumina. The very high PS selectivity values observed for all the samples of Table 3 show that the conversion of citral via other reactions than its condensation with acetone is negligible. Consistently, Noda Pérez et al. [15] reported that products from the self-condensation of citral are formed only in trace amounts on a Mg_4AlO_x sample. On the other hand, Table 3 also shows that the cis-PS/trans-PS ratio slightly increased with the Al content on Mg_yAlO_x samples, from 1.26 on Mg_3AlO_x to 1.62 on $Mg_{0.11}AlO_x$.

The initial DMK conversion rates (r_{DMK}^0, μmol/min m^2) were determined from the initial slopes of X_{DMK} vs (tW/n_{DMK}^0) curves (not shown here), similarly to citral in Fig. 5. Results are presented in Table 4. The r_{DMK}^0 values on Mg_yAlO_x samples increased with the Al content, following an opposite trend in comparison to that

observed for r_{Cit}^0 values in Table 3. Consistently, r_{DMK}^0 was more than two times higher on Al_2O_3 than on MgO. Table 4 also shows the initial selectivities obtained for the DMK-derived products; DAA and MO are formed via the self-condensation of DMK, and PS from the citral/DMK cross-condensation. MO was initially a minor product on all the samples while the initial selectivity to DAA was always clearly higher than that to PS. On Mg_yAlO_x samples, S_{DAA}^0 increased with the Al content at the expense of PS, from 64.6% on Mg_3AlO_x to 85.9% on $Mg_{0.11}AlO_x$. This result shows that on Mg_yAlO_x samples the observed increase of r_{DMK}^0 with the Al content essentially reflects the increase of the DAA formation rate.

3.3. Sample composition, surface acid–base properties and reaction mechanism

Results of Tables 3 and 4 showed that the initial conversion rates of DMK and citral on Mg_yAlO_x depend on the sample composition, following opposite trends: r_{DMK}^0 increases while r_{Cit}^0 diminishes with the Al content. In Fig. 6 we have plotted the initial formation rates of PS and DAA, the main products derived from citral and DMK, respectively, as a function of the Al/(Al + Mg) ratio. It is observed that the r_{PS}^0 curve shows a slight maximum for Mg_3AlO_x sample. On MgO and Mg_3AlO_x, r_{DAA}^0 was about 9 μmol/min m^2, slightly higher than r_{PS}^0 ($\approx$6 μmol/min m^2). Then, r_{DAA}^0 increased while r_{PS}^0 diminished with increasing Al/(Al + Mg) ratios. Thus, for Al/(Al + Mg) = 0.9 ($Mg_{0.11}AlO_x$ sample) the r_{DAA}^0 value reached about 25 μmol/min m^2 while r_{PS}^0 decreased to 0.6 μmol/min m^2. These results clearly show that not only the activity but also the selectivity of the citral/DMK reaction on Mg_yAlO_x mixed oxides depend on the sample composition.

In an attempt to correlate the catalytic behavior of Mg_yAlO_x samples with their surface acid–base properties and to gain insight into the reaction mechanism, we compared the r_{DAA}^0 and r_{PS}^0 data with the density of acid and base sites given in Table 2. A linear plot was obtained when r_{PS}^0 was represented as a function of the density of strong base sites (n_O, μmol/m^2), as shown in Fig. 7. In contrast, a

Table 4
Catalytic results for the citral/DMK reaction on Mg_yAlO_x, MgO and Al_2O_3 samples (DMK-derived products)

Catalyst	Initial DMK conversion rate, r_{DMK}^0 (μmol/min m^2)	Initial selectivities (%)		
		S_{MO}^0	S_{DAA}^0	S_{PS}^0
MgO	14.4	0.8	66.6	32.6
Mg_3AlO_x	13.3	6.0	64.6	29.4
Mg_1AlO_x	14.6	2.9	72.0	25.1
$Mg_{0.5}AlO_x$	22.5	1.7	80.0	18.3
$Mg_{0.33}AlO_x$	21.8	0.8	84.1	15.1
$Mg_{0.2}AlO_x$	23.0	2.0	83.2	14.8
$Mg_{0.11}AlO_x$	28.5	2.2	85.9	11.9
Al_2O_3	35.0	2.1	83.3	14.6

Table 3
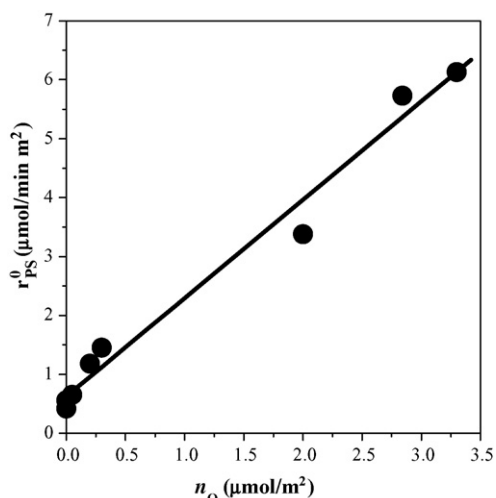Catalytic results for the citral/DMK reaction on Mg_yAlO_x, MgO and Al_2O_3 samples (citral-derived products)

Catalyst	Initial citral conversion rate, r_{Cit}^0 (μmol/min m^2)	Citral conversion[a], X_{Cit} (%)	PS selectivity[a], S_{PS} (%)	cis-PS/trans-PS ratio[a]
MgO	6.1	89.0	96.6	1.43
Mg_3AlO_x	7.9	87.0	96.5	1.26
Mg_1AlO_x	3.4	52.5	100.0	1.42
$Mg_{0.5}AlO_x$	1.5	61.3	93.0	1.41
$Mg_{0.33}AlO_x$	0.8	51.9	91.0	1.50
$Mg_{0.2}AlO_x$	1.5	44.9	93.0	1.52
$Mg_{0.11}AlO_x$	0.7	33.1	90.0	1.62
Al_2O_3	0.6	30.3	97.8	1.60

Reaction conditions: $T = 353$ K, $n_{DMK}^0 = 0.8$ mol, $n_{Cit}^0 = 0.016$ mol, $W_{Cat.} = 0.5$ g.
[a] At 6 h.
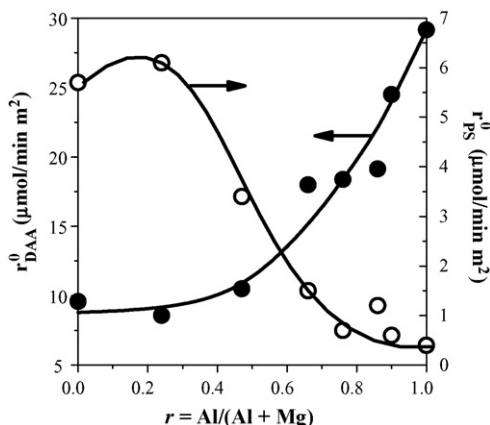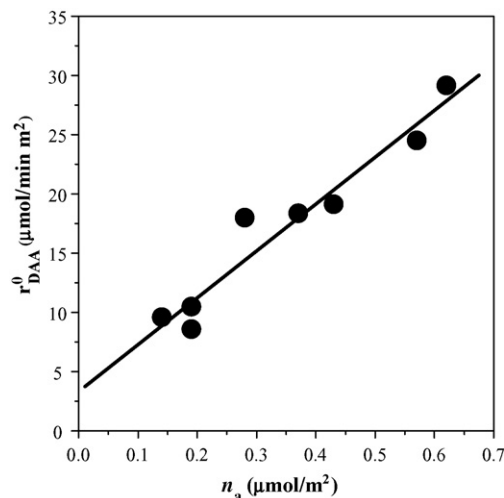
Fig. 6. Initial formation rates of DAA and PS as a function of the sample composition (T = 353 K, n_{DMK}^0 = 0.8 mol, n_{Cit}^0 = 0.016 mol, $W_{Cat.}$ = 0.5 g).

Fig. 8. Initial DAA formation rates on Al_2O_3, Mg_yAlO_x and MgO catalysts as a function of acid site density. Reaction conditions as in Fig. 6.

Fig. 7. Initial PS formation rate on Al_2O_3, Mg_yAlO_x and MgO catalysts as a function of strong base site density. Reaction conditions as in Fig. 6.

poor correlation was found when r_{PS}^0 was represented against the density of weak (n_{OH}) or medium-strength (n_{MO}) basic sites. The observed proportionality between r_{PS}^0 and n_O in Fig. 7 indicates that under initial conditions, the rate-determining step for the citral/DMK reaction toward PS is promoted by strongly basic O^{2-} sites, which is in agreement with our previous results obtained on Li-modified MgO catalysts [13]. The function of surface O^{2-} sites is to abstract the α-proton from acetone, forming a carbanion that consecutively attacks the carbonyl group of the contiguously

adsorbed citral molecule, as depicted in Scheme 2. Then a β-hydroxyl ketone intermediate is expected to form; however, this was never observed among the reaction products under the reaction conditions of this work. Therefore, this unstable intermediate is assumed to rapidly dehydrate, forming PS and water and regenerating the active sites on the catalyst surface. The roles of surface Mg^{2+} and Al^{3+} sites are to provide adsorption sites for DMK through its carbonyl group and to stabilize the reaction intermediates.

Regarding the DAA formation, a good correlation was obtained between r_{DAA}^0 and the total surface acid site density (n_a, μmol/m²), as shown in Fig. 8. Taken into account that the IR spectra of adsorbed pyridine showed that Mg_yAlO_x samples contain essentially Lewis acidity, the results in Fig. 8 strongly suggest that the self-condensation of DMK to DAA is promoted by surface Al^{3+} and Mg^{2+} cations. Nevertheless, even on very poorly acidic MgO and Mg_3AlO_x samples, DMK is converted to DAA at high rates, r_{DAA}^0 being higher than r_{PS}^0 on these samples, as previously noted. The latter indicates that the formation of DAA from DMK is also catalyzed by base sites. In a previous paper [13], we proposed that the self-condensation of DMK to DAA takes place on strongly basic O^{2-} sites as depicted in the mechanism of Scheme 3. The self-condensation of DMK occurs initially by the formation of the carbanion intermediate via the abstraction of α-proton from acetone, as illustrated in Scheme 2 for the PS synthesis; i.e., the formation of DAA and PS on base sites proceeds via parallel reaction pathways that share the common carbanion intermediate.
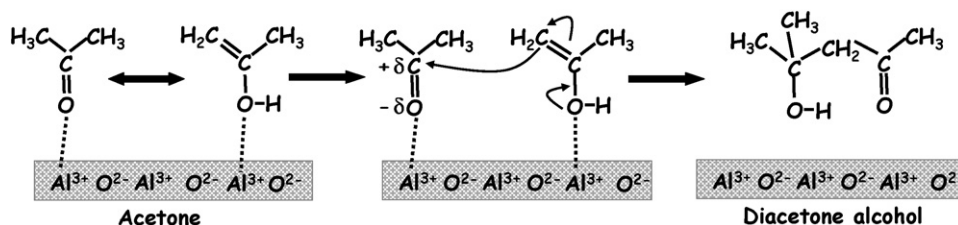
Nevertheless, results in Fig. 8 showed that the DMK conversion to DAA also occurs via a reaction mechanism promoted by surface
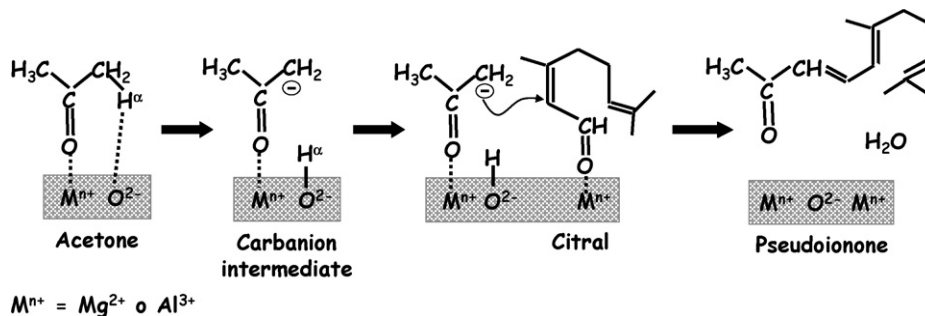
Scheme 2. Pseudoionone formation mechanism in citral/acetone reaction.
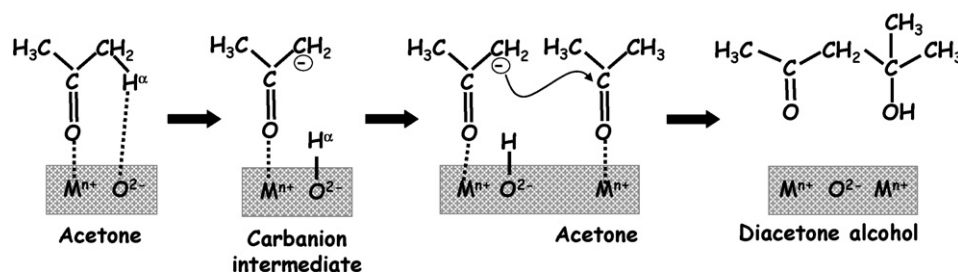
Scheme 3. Diacetone alcohol formation mechanism on MgO and Mg-rich Mg_yAlO_x samples.

Scheme 4. Diacetone alcohol formation mechanism on Al_2O_3 and Al-rich Mg_yAlO_x samples.

acid sites. Acid-catalyzed aldol condensation of ketones has been particularly studied on acid zeolites such as HZSM-5 [35,36]. Xu et al. [35] claimed that the formation of a reactive complex between the ketone and the Brönsted acid sites of the zeolite is implicated as a precursor of the condensation reactions at low temperature. The DMK condensation has also been investigated on non-zeolitic materials containing essentially Lewis acidity. For example, Panov and Fripiat [37] studied the reaction on alumina by FTIR technique. They reported that the DMK conversion to DAA is much faster on alumina than on acid zeolites and suggested that the surface Lewis sites on alumina activate the acetone molecule forming an enol that reacts with an acetone molecule in gas-phase. Biaglow et al. [38] stated that the DMK condensation in dealuminated faujasites occurs on non-framework alumina via a similar mechanism to the one that takes place on the surface Lewis sites of activated alumina. Based on these previous reports, and taken into account that the pyridine spectra of Fig. 3 showed that the Brönsted acidity in $Mg_{0.2}AlO_x$ and Al_2O_3 is very weak, we propose that the acid-catalyzed DMK condensation on Mg_yAlO_x samples occurs on surface Lewis acid sites following the reaction mechanism depicted in Scheme 4. The DMK molecule in equilibrium with the enol tautomer is activated on Lewis M^{n+}

sites via the oxygen of the C=O group generating an electrophilic carbonyl carbon. Then, the enol form that is nucleophilic at the α-carbon attacks the electrophilic carbonyl carbon leading to diacetone alcohol. The DMK interaction with the solid surface in Scheme 4 would involve essentially stronger Lewis acid sites, i.e., Al^{3+} sites, as it is clearly suggested by the observed r^0_{DAA} increase with the Al content of Mg_yAlO_x samples in Fig. 6.

Contrarily to self-condensation of DMK, the cross-condensation of citral with DMK was not promoted on Mg_yAlO_x acid sites. Probably, the interaction of the electrodonor groups of the citral molecule (C=C and C=O) with more electronegative Al^{3+} Lewis acid sites is strong enough to prevent the reaction of the adsorbed aldehyde with the acetone intermediate at measurable rates. Previous work has shown, in fact, that the citral/DMK cross-aldolization on Mg–Al catalysts is negative order with respect to citral which reflects the stronger adsorption of citral in comparison to acetone [8].

3.4. Catalyst deactivation

The in situ catalyst deactivation was studied on selected samples of Table 1 by performing two consecutive catalytic tests
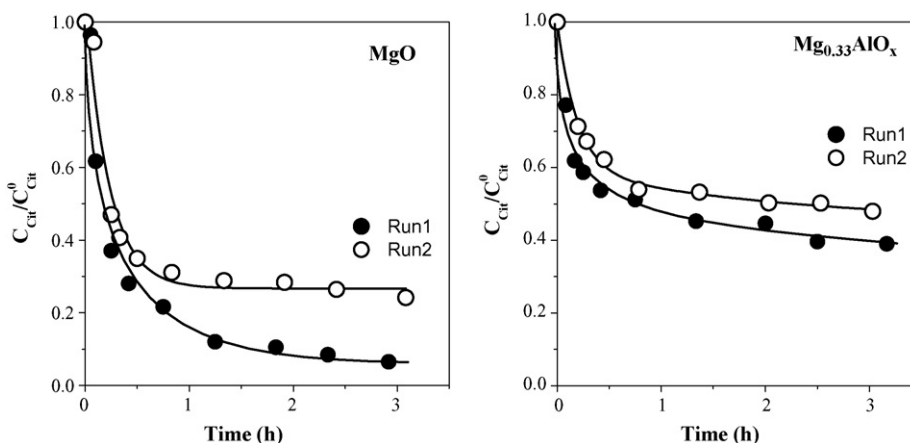

Fig. 9. Consecutive catalytic runs to evaluate in situ catalyst deactivation ($T = 353$ K, $n^0_{DMK} = 0.8$ mol, $n^0_{Cit} = 0.016$ mol, $W_{Cat.} = 0.7$ g).

without stopping the run. The procedure was as follows: after 3 h of a standard run at 250 kPa, an additional amount of citral was introduced so that the total moles of citral in the reactor were equivalent to the initial moles of citral loaded to the reactor, n_{Cit}^0, and a second consecutive run was performed. Results obtained with MgO and $Mg_{0.33}AlO_x$ samples are shown in Fig. 9. On MgO, the citral concentration decay rate was slower in the second run in comparison with the first one, reflecting the partial sample deactivation. The citral conversion after 3 h run was 94% in the first test and 76% in the second one; i.e., the relative activity lost was about 20%. Sample $Mg_{0.33}AlO_x$ also deactivated during the citral/DMK reaction. Citral conversion values of 61% and 52% were obtained on $Mg_{0.33}AlO_x$ after the 3 h run in the first and second catalytic tests, respectively. Similar consecutive catalytic tests carried out on Mg_1AlO_x and $Mg_{0.2}AlO_x$ samples (not shown here) confirmed that the relative activity lost was between 15 and 20%. The observed deactivation of Mg_yAlO_x samples during the citral/DMK reaction is probably caused by the presence of carbonaceous deposits formed from the strong adsorption of reactants and/or products, in particular, citral. Therefore, one can expect that the deactivation of Mg_yAlO_x samples increases when the citral concentration in the feed is increased.

4. Conclusions

The surface acid/base properties of Mg_yAlO_x samples essentially depend on chemical composition. Strongly basic O^{2-} sites and surface Mg–O pairs are dominant on MgO and Mg_yAlO_x samples with Al/(Al + Mg) atomic ratios lower than 0.5. In Al-rich samples, the relative contribution of strong and middle base sites decreases with increasing the Al content at the expense of weak base sites. The surface acid site density is similarly low on Mg-rich samples, but increases almost linearly with increasing Al content on samples with Al/(Al + Mg) > 0.5.

The rates and product distributions for citral/acetone reactions are also strongly influenced by the composition of Mg_yAlO_x samples. The cross-aldol condensation of citral with acetone to yield pseudoionones is promoted on MgO and MgO-rich Mg_yAlO_x samples because these samples contain a much large number of strongly basic O^{2-} sites, which detach the α-proton from the acetone molecule and form a carbanion intermediate in the rate-determining step. Initial formation rates of pseudoionones are very low on Al_2O_3 and Al-rich samples showing that the citral/acetone condensation reaction does not occur via acid-catalyzed mechanisms.

The parallel formation of diacetone alcohol from the self-condensation of acetone takes place on strong base sites, sharing the carbanion intermediate with the pseudoionone formation

mechanism. However, the condensation of acetone to diacetone alcohol is also efficiently catalyzed on more electronegative Lewis Al^{3+} sites which activate the acetone molecule via the oxygen of the C=O group generating an electrophilic carbonyl intermediate. Thus, the initial formation rate of diacetone alcohol on Mg_yAlO_x samples increases markedly with the Al content. The abundance of surface Al^{3+} sites accounts for the high diacetone alcohol formation rates observed on Al_2O_3 and Al-rich Mg_yAlO_x samples.

References

[1] Ullman's Encyclopedia of Industrial Chemistry, sixth edition, 2002 electronic release.
[2] E. Brenna, C. Fuganti, S. Serra, P. Kraft, Eur. J. Org. Chem. (2002) 967.
[3] P. Gradeff, US Patent 3,840,601 (1974) to Rhodia Inc.
[4] P. Mitchell, US Patent 4,874,900 (1989) to Union Camp Corporation.
[5] P.Z. Bedoukian, Perfumery and Flavoring Synthetics, Elsevier, New York, 1967, p. 99.
[6] E.G. Craven, J. Appl. Chem. 13 (1963) 71.
[7] M.J. Climent, A. Corma, S. Iborra, A. Velty, Catal. Lett. 79 (2002) 157.
[8] J.C. Roelofs, A.J. van Dillen, K.P. de Jong, Catal. Today 60 (2000) 297.
[9] M.J. Climent, A. Corma, S. Iborra, K. Epping, A. Velty, J. Catal. 225 (2004) 316.
[10] S. Abelló, F. Medina, D. Tichit, J. Pérez-Ramírez, X. Rodríguez, J.E. Sueiras, P. Salagre, Y. Cesteros, Appl. Catal. A 281 (2005) 191.
[11] S. Abelló, S. Dhir, G. Colet, J. Pérez-Ramírez, Appl. Catal. A: Gen. 325 (2007) 121.
[12] E.L. Jablonski, I.M.J. Vilella, S.C. Maina, S.R. de Miguel, O.A. Scelza, Catal. Commun. 7 (2005) 18.
[13] V.K. Díez, C.R. Apesteguía, J.I. Di Cosimo, J. Catal. 240 (2006) 235.
[14] C. Noda Pérez, C.A. Pérez, C.A. Henriques, J.L.F. Monteiro, Appl. Catal. A: Gen. 272 (2004) 229.
[15] C. Noda Pérez, C.A. Henriques, O.A.C. Antunes, J.L.F. Monteiro, J. Mol. Catal. A: Chem. 233 (2005) 83.
[16] P. Kustrowski, D. Sulkowska, L. Chmielarz, R. Dziembaj, Appl. Catal. A: Gen. 302 (2006) 317.
[17] J.I. Di Cosimo, V.K. Díez, C.R. Apesteguía, Appl. Clay Sci. 13 (1998) 433.
[18] S. Velu, C.S. Swamy, Catal. Lett. 40 (1996) 265.
[19] A. Corma, S. Iborra, J. Primo, F. Rey, Appl. Catal. 114 (1994) 215.
[20] B.M. Choudary, M.L. Kantam, C.R.V. Reddy, K.K. Rao, F. Figueras, J. Mol. Catal. A: Chem. 146 (1999) 279.
[21] P. Kumbhar, J. Sanchez-Valente, F. Figueras, J. Chem. Soc., Chem. Commun. (1998) 1091.
[22] H. Schaper, J.J. Berg-Slot, W.H.J. Stork, Appl. Catal. 54 (1989) 79.
[23] J.I. Di Cosimo, V.K. Díez, M. Xu, E. Iglesia, C.R. Apesteguía, J. Catal. 178 (1998) 499.
[24] J.I. Di Cosimo, C.R. Apesteguía, M.J.L. Ginés, E. Iglesia, J. Catal. 190 (2000) 261.
[25] J.I. Di Cosimo, G. Torres, C.R. Apesteguía, J. Catal. 208 (2002) 114.
[26] A. Corma, V. Fornés, F. Rey, J. Catal. 148 (1994) 205.
[27] V.K. Díez, C.R. Apesteguía, J.I. Di Cosimo, J. Catal. 215 (2003) 220.
[28] R. Philipp, K. Fujimoto, J. Phys. Chem. 96 (1992) 9035.
[29] C. Morterra, G. Ghiotti, F. Boccuzzi, S. Coluccia, J. Catal. 51 (1978) 299.
[30] T. Kanno, M. Kobayashi, in: M. Misono, Y. Ono (Eds.), Acid–Base Catalysts II, Elsevier, Kodansha, 1994, p. 207.
[31] E.P. Parry, J. Catal. 2 (1963) 371.
[32] C. Monterra, G. Magnacca, Catal. Today 27 (1996) 497.
[33] S. Damyanova, P. Grange, B. Delmon, J. Catal. 168 (1997) 421.
[34] G. Busca, Catal. Today 41 (1998) 191.
[35] T. Xu, E.J. Munson, J.F. Haw, J. Am. Chem. Soc. 116 (1994) 1962.
[36] A.I. Biaglow, J. Sepa, R.J. Gorte, D. White, J. Catal. 151 (1995) 373.
[37] A.G. Panov, J.J. Fripiat, J. Catal. 178 (1998) 188.
[38] A.I. Biaglow, R.J. Gorte, D. White, J. Catal. 150 (1994) 221.